Materials Advances

ROYAL SOCIETY OF CHEMISTRY

PAPER

View Article Online
View Journal | View Issue

Cite this: *Mater. Adv.*, 2023, 4, 4537

A Multifunctional tannic acid–Fe^{3+}–graphene oxide loaded alginate photothermal network: an interfacial water evaporator, a disinfector and a power generator†

M. Amarnath,[a] Hirakendu Basu,*[ab] Ranita Basu,[bc] Pallavi Chandwadkar,[d] Celin Acharya,[bd] Shweta Singh,[ab] Suresh Kumar Kailasa[e] and Chandra Nath Patra[ab]

The development of efficient photothermal materials with multifunctional capabilities is considered an effective approach for utilizing abundant free solar energy and exploring new concepts for prospective sustainable energy and environmental applications. A facile stepwise synthesis strategy for a tannic acid–Fe^{3+}–graphene oxide impregnated alginate photothermal network (TA–Fe^{3+}–GO–ALG) was developed through sonication assisted loading of tannic acid and Fe^{3+} into graphene oxide layers followed by impregnation of the whole assembly into an alginate polymeric network. The portable device fabrication involves simply coupling the developed TA–Fe^{3+}–GO–ALG with a specially shaped water floater material. The TA–Fe^{3+}–GO–ALG photothermal material exhibited remarkable proficiency of light to heat transformation of 87% under 0.5 sun solar illumination. The rate of water evaporation under favourable circumstances attained a maximum of 1.8 kg m^2 h^{-1}, indicating great feasibility for its implementation as a solar water purifier. The TA–Fe^{3+}–GO–ALG photothermal material displayed excellent stability, recyclability, no photo leaching under different aquatic environments and could effectively produce potable water from real seawater and other simulated wastewater. A maximum increase of 70 °C in water temperature under 2 sun irradiation was achieved for sea water. Moreover, the developed TA–Fe^{3+}–GO–ALG material also showed exceptional antibacterial efficacy towards *E. coli*, eradicating nearly 100% of bacteria when exposed to 0.5 solar irradiation. Spot assays as well as viability counts indicated the superior antimicrobial properties. The excellent photo-thermal conversion efficiency integrated with the Bi_2Te_3 based commercial thermoelectric module exhibited a good photo-thermoelectric effect. Its significant generation of Seebeck voltage has opened up avenues for its application towards solar-to-electricity conversion. Our effort delivers novel insights into the rational strategy of benchmark TA–Fe^{3+}–GO–ALG based floatable photothermal devices with interfacial water evaporation, antimicrobial properties for sustainable water treatment and power generation through the photo-thermoelectric effect.

Received 13th July 2023,
Accepted 24th August 2023

DOI: 10.1039/d3ma00408b

rsc.li/materials-advances

1. Introduction

The broad quest for novel nano-enabled photothermal materials is now recognised as a new frontier area of study with multiple high-potential impacts on energy and environment applications.[1] The exclusive size dependent broad solar spectrum absorption, low reflection and excellent light to heat conversion capabilities of various nano dimensional structures indicate unique optical and thermal properties. Photons from the radiation of sun consist of the whole electromagnetic spectrum, selected frequencies from which are directly absorbed by the photothermal materials owing to their intrinsic electronic, bandgap assembly which results in the

[a] *Analytical Chemistry Division, Bhabha Atomic Research Centre, Trombay, Mumbai – 400085, India. E-mail: hirak@barc.gov.in; Fax: +91-22-25595151; Tel: +91-22-69290312*
[b] *Homi Bhabha National Institute, Anushaktinagar, Mumbai – 400094, India*
[c] *Technical Physics Division, Bhabha Atomic Research Centre, Trombay, Mumbai – 400085, India*
[d] *Molecular Biology Division, Bhabha Atomic Research Centre, Trombay, Mumbai – 400085, India*
[e] *Department of Chemistry, Sardar Vallabhbhai National Institute of Technology, Surat – 395007, India*

† Electronic supplementary information (ESI) available. See DOI: https://doi.org/10.1039/d3ma00408b

transformation of light energy to beneficial heat energy for various applications such as water evaporation, purification, catalysis, electricity generation, sterilization, *etc.*[2]

With the rise of nanotechnology, a wide range of photothermal materials have been reported. Nanoparticle loaded two-dimensional (2D) photothermal nanostructures have gained significant attention due to their exceptional insulation properties, low enthalpy of water loss, and stereo-convective flow. High efficiency in photothermal conversion can be achieved with modification in their surface structure. Engineered nanostructures may promote maximum light absorption and heat conversion.[3] Inorganic metallic nanoparticles,[4] semiconductors,[5] carbon derivatives,[6] organic polymers,[7] and 2D transition metal carbide/nitride based hybrids[8] are examples of such nanostructures. From those photothermal materials graphene oxide (GO) comprises a 2D layer structure which consists of stacked hexagonally arranged carbon atoms and has been shown to have good photothermal properties.[9] Tannic acid (TA) is a natural photosensitizer, which absorbs photons and transfers energy to the surrounding environment. TA comes under the polyphenol family which can be found in various plant species such as tea, coffee, and wine. Its non-toxicity, low cost, and simple manufacturing technique make it an appealing material for sustainable environmental solutions.[10] Efficient utilization of the vast electromagnetic region towards photothermal conversion may not be achievable only through organic nanostructures. One approach to overcome this issue is to incorporate suitable metals or metal oxides. Fe^{3+} is such an ion which withstands prolonged exposure to sunlight without degrading the photothermal device.[11] It acts as a catalyst for the photo-oxidation of water molecules, which generates heat and causes evaporation. Fe^{3+} can be incorporated into the base layer of GO and TA. Fe^{3+}, when suitably doped into the graphene layer, can exhibit excellent photothermal capability due to the favourable band structure. Efficient binding of these GO, TA, and Fe^{3+} together is essential for floatable framework formation. Alginate is a naturally occurring polymer which can be utilized due to its physical cross-linking propensity with sol–gel changeover in the presence of multivalent cations (*e.g.* Ca^{2+}). Loading efficient nano enabled photothermal materials into the alginate network provides important advantages like shielding the nanomaterials into polymeric structures preventing their unwanted release into the surrounding environment, through water permeability with capillary action.[12,13]

An appropriately designed photothermal structure can exhibit multifunctional properties and can have wide applications *viz.* steam generation by photothermal heating followed by condensation to produce clean water; an antimicrobial effect and electric power generation using the photo-thermoelectric effect when integrated with the thermoelectric module.[14] Potable water can be produced *via* a variety of methods that include distillation, reverse osmosis, filtration, chlorination, UV radiation and chemical treatment.[15,16] Among the above mentioned methods solar driven distillation is the most convenient and cost effective one. Photothermal assisted solar water evaporation is a powerful method for removing impurities from water, such as pathogens, viruses, minerals, and toxins. With few moving parts, distillation equipment is comparatively basic and does not suffer from heat loss unlike bulk evaporation systems. To enhance sunlight absorption, the approach of using light-absorbing particles in water and interfacial heating approach has been described by many researchers.[9] Fathi S. Awad *et al.*, conveyed the preparation methods of graphene and polyurethane based nanocomposites. Under 1, 5, and 8 sun irradiation, the Au/Ag–PGPU foams have typical water evaporation rates of 1.00, 6.59, and 11.34 kg m^{-2} h^{-1}, with excellent solar conversion efficiencies of up to 63%, 88%, and 96.5%.[17] Laila Noureen *et al.*, prepared Ag_3PO_4–rGO nanocomposite-coated fabrics and attained a high water evaporation amount of 1.31 kg m^2 h^{-1}.[18] Wu *et al.*, developed magnetic Fe_3O_4 nanoparticles with GO and it exhibits a high evaporation rate of 1.12 L h^{-1} and a conversion efficiency of 70% under 1 sun illumination.[19]

The threat of bacterial and viral diseases to public health remains high and researchers face ongoing challenges. Despite the seriousness of the antimicrobial resistance problem, the development and approval of new antibiotics and antiviral drugs is uncommon in the modern era. Nanomaterial-based light treatments have been employed as a highly effective method of disinfecting bacterial pathogens, with the utilization of nanocomposites being particularly noteworthy and even more relevant in the post COVID-19 era. Generally under solar illumination, the photothermal material results in an escalated degradation of the microbial cell envelope. This was attributed to the heat produced by the photothermal effect, which causes protein coagulation and subsequent deterioration of the bacterial cell envelope.[20] Nanostructures exhibiting highly efficient photothermal behaviour for bacteria killing are particularly advantageous owing to their minimally invasive nature, remote controllability, and exceptional efficiency. An appropriately designed nano enabled photothermal material can show dual functionality by cleaning waste water from contaminants through evaporation and distillation as well as by killing pathogens simultaneously. Few materials have been reported with these dual characters.[21]

In the prevalent energy landscape, exploiting solar radiation is of utmost importance and in this regard, a photovoltaic module using crystalline silicon (c-Si) is used with multiple advantages *viz.*, easy processing, enhanced power conversion efficiency, *etc.*[22] However, it suffers limitation owing to the energy band gap of 1.12 eV of Si at 300 K. Theoretically, it allows absorption of photons with wavelengths up to 1100 nm. Moreover, 40% of the total solar radiation consists of wavelengths higher than 1100 nm and so to raise the performance of the PV module it is necessary to tap the broad spectrum of phonons preferably at $\sim$2500 nm.[20] Fraunhoffer in 2014 fabricated a PV module of a four-junction cell of GaInP/GaAs//GaInAsP/GaInAs wafer with the aim of utilizing the full spectrum. Nevertheless, due to cost-ineffectiveness, the concept was unsuitable for mass production.[23] An alternative approach to harness solar energy is the integration of a photothermal material (light absorber) and

thermoelectric modules to make a hybrid power generator utilising the concept of the photo-thermoelectric effect.[24] This configuration permits the broad spectrum of solar radiation to be utilized. The use of a single photothermal material or device with multifunctional roles like pollutant decontamination, pathogen disinfection and power generation is a revolutionary concept which upon successful materialisation can have enormous impact on energy and environmental science.

In this current study, we present a novel multifunctional photothermal network of tannic acid–Fe^{3+}–graphene oxide loaded alginate (TA–Fe^{3+}–GO–ALG). We have optimized the performance by optimum loading of Fe^{3+} and TA over the GO surface for a highly efficient photothermal effect. The developed material was characterised by XRD, FTIR, Raman, DLS, SEM and TEM for structural and morphological analysis. A floatable water evaporator system based on the developed material was designed. The evaporator performs well in solar water vaporisation and distillation in line for the combination of the efficient 2D structure (TA–Fe^{3+}–GO–ALG). The light to heat transformation proficiency and water evaporation level under different circumstances were evaluated. Purification efficiencies for sea water and lake water in the presence of organic dyes were tested under different solar illumination conditions. The antibacterial efficacy of the developed photothermal material was tested through spot assays as well as viability counts. The performance of the photothermal material was integrated with a Bi_2Te_3 based thermoelectric module to evaluate its applicability towards solar-to-electricity conversion apart from its ability to produce clean water.

2. Materials and methods

2.1 Materials

All of the chemicals and reagents utilised in this investigation were of analytical grade and were utilised without additional purification. Double distilled (DD) water was used during the course of the sample preparations. Natural graphite flakes and tannic acid were purchased from Sigma-Aldrich. Ferric chloride and potassium permanganate were procured from Sisco Research Laboratories Private Limited. Sulphuric acid, orthophosphoric acid, hydrochloric acid, hydrogen peroxide, and ethanol were purchased from Advent Chembio Private Limited.

2.2 Synthesis of the photothermal material

The synthesis of the desired materials for assessing the photothermal behaviour was carried out in multiple steps which are discussed here.

2.2.1 Synthesis of GO. The preparation of GO was achieved using an improved Hummers' method.[25] Briefly, 3 g (1 wt%) of pure graphite powder was taken in 400 mL of 9 : 1 fusion of H_2SO_4 and H_3PO_4 and stirred for 30 min. A homogeneous mixture of graphite dispersion was obtained then 18.0 g (6 wt%) of $KMnO_4$ was added gradually to maintain the temperature under 50 °C. The shift in colour of the fluid from black to green indicates an exothermic reaction triggered by the exfoliation of the highly ordered graphite stacks. The reaction was kept overnight for 12 h. Then the colour of the solution changes from green to mild pink. 5 mL of H_2O_2 (30%) was added with 400 mL of ice cubes and added to the above solution to end the reaction. The yellow color solution was kept in a centrifuge at 7000 rpm and washed with 30% HCL, ethanol and water. Finally, the precipitate was dried at 80 °C.

2.2.2 Loading of Fe^{3+} on GO sheets. In a typical experiment 0.1 g of GO was taken in 30 mL DD and retained in bath sonication for 30 min and kept for stirring at 400 rpm. 0.05 g of $FeCl_3$ was taken and added in 30 mL DD water separately. Then, the solution was transferred dropwise into the GO dispersion and the temperature was increased to 50 °C. For reduction of $FeCl_3$ to Fe^{3+} the pH of the solution was increased to 10 by adding aqueous ammonia. The colour of the solution turned to dark black indicating the formation of Fe^{3+} and the temperature was increased to 85 °C. Finally the precipitate was centrifuged and washed several times with ethanol, DD water and dried for the next step.[10]

2.2.3 Synthesis of the TA–Fe^{3+}–GO photothermal material. For evaluating the photo thermal behaviour of the prepared nanocomposites TA and Fe^{3+} were functionalized over the GO surface with a number of different wt%. Initially, for the composite namely PT-1, 0.5 g of GO was placed in 30 mL of DD water and kept in bath sonication for 15 min. 0.1 g of TA was placed in 1 mL DD water and added to the GO dispersion slowly at 400 rpm stirring. 1 mL of DD water was mixed with 0.1 g of $FeCl_3$ and added to the aforementioned solution. Ammonia solution was used to increase the pH to 9. After adding, the solution was vigorously stirred for another 1 h for the successful functionalization of Fe^{3+} over the TA and GO. Lastly the precipitate was filtered and washed with DD and dried at 80 °C. The same procedure was followed for the preparation of the other nanocomposites namely PT-2 to PT-5. Another set of nanocomposites was prepared using the same method discussed above to investigate the behavioural change of the solar absorber towards various TA loading keeping the GO and Fe^{3+} ratio constant. A constant amount of GO (0.5 g) and $FeCl_3$ (0.2 g) was taken and the loading of TA was varied from 0.1 g to 0.5 g. The nanocomposites were named as PT-6 to PT-10. A table showing the composition of all the developed photothermal materials is presented in the ESI† (Table S1).

2.2.4 Impregnation of TA–Fe^{3+}–GO into the alginate network. A facile and efficient dipping method was used for the water evaporator sample preparation. 4 wt% sodium alginate powder was dissolved in 100 mL DD water and mixed for 1 hour. 4 wt% of $CaCl_2$ was taken and added in the 100 mL DD water. 1 g of prepared materials (PT-1 to PT-10) were added to the alginate gel and mixed well to obtain a uniform distribution throughout the gel. The prepared cotton fibre was immersed into the prepared gel for the adsorption of materials throughout the cotton fibres. The immersion was allowed for a period of 10 min and simultaneously it was dipped into the $CaCl_2$ solution. The material was allowed to be inside the $CaCl_2$ solution for another 1 h. Finally the

material (TA–Fe^{3+}–GO–ALG) was taken and washed multiple times for further evaluation studies.[12]

2.2.5 Fabrication of a floatable device. After successful synthesis of the desired materials TA–Fe^{3+}–GO–ALG, it was incorporated suitably into a foam floater to fabricate a compact photothermal device. A user friendly foam material was taken and the required area (2 cm^2) for the solar absorber material loading was removed. The surrounding and the bottom surface of the prepared material was now able to be always in contact with water which makes it an appropriate interfacial water evaporator material. The changes in solar absorption and heat transfer at the gap between the material and foam shows the effectiveness of the prepared material towards various solar illuminations.

2.3 Photo thermal behaviour assessment test

Photothermal behaviour assessment for all the prepared materials (TA–Fe^{3+}–GO–ALG: PT-1 to PT-10) was carried out using the solar simulator with varied intensity (0.1 to 1 sun) accordingly. The mass loss of water was used to calculate water evaporation during photothermal activity by using an electronic balance Wensar class 1 weighing scale. GO, GO–Fe^{3+}, and all PT series components were coated and made to float on the surface of 400 mL of water in a beaker. The external temperature was then monitored by employing an infrared camera at various times. For the water evaporation tests, the temperature and humidity were taken at ambient temperature with 40% RH. The intensity of indoor solar illumination was determined by the Lutron Instrukart LX-101A Digital lux metre. Underground wastewater samples have been modified to replicate acidic water (0.1 M HCl) and alkaline water (0.1 M NaOH). Three different organic dye solutions containing 50 mg L^{-1} concentration of methyl orange, methyl red and rhodamine B were taken as model pollutants to assess the real time efficiency of wastewater evaporation and purification. Sea water samples were collected from the Arabian Sea at Trombay jetty and lake water samples were collected from Virar lake, Mumbai, Maharashtra, India. Both water samples were added with methyl orange dye at a concentration of 50 mg L^{-1} and its evaporation and distillation rate were identified. The fresh water from all the dye mixed underground, sea and lake water samples was tested using an Orion star A111, Thermo scientific pH meter. The absorption maximum of pollutants was examined using a UV-vis spectrometer. The heavy metal concentrations were identified using Horiba scientific Ultima expert inductively coupled plasma-optical emission spectrometry. Outdoor water evaporation was carried out from 1st May to 6th May 2023 on bright days from 10 am to 5 pm at BARC, Trombay, Mumbai.

2.4 Photothermal antimicrobial assessment test

Mid log phase cells of *E. coli* were used to assess the antimicrobial properties of TA–Fe^{3+}–GO–ALG (PT-2). The cell equivalent to 1 OD 600 nm cells were washed with distilled water and inoculated in a beaker containing 100 mL of distilled water with floater PT-2. Aliquots of *E. coli* were withdrawn from the beaker at 0 h and 4 h. Cells were serially diluted (*i.e.* 100, 10^{-2}, 10^{-4}) and spotted onto an LB agar plate and incubated under the usual growth conditions. Cells were also spread on LB agar plate to determine the number of colonies in terms of CFU mL^{-1} at 10^{-5} dilution after 0 h and without dilution after 4 h of incubation. The cell morphology of *E. coli* was examined under a scanning electron microscope (SEM) at 0 h and 4 h. For this, cells were immobile with 2.5% glutaraldehyde at 4 °C for 1 h. The resulting cells were then consecutively dried out with 20, 30, 50, 70, 90, and 100% ethanol for 2 min each at room temperature.

2.5 Preparation of a light absorber on the thermoelectric module

First, the top surface of the thermoelectric module was cleaned with dust-free cloth. Subsequently, the light absorbing TA–Fe^{3+}–GO–ALG (PT-2) material was placed on the thermoelectric module with thermal paste in order to eliminate the air gaps between them. Light to electricity generation using the concept of photo-thermoelectricity was conducted under 0.5 sun that was pre-calibrated using a certified Si photodiode cell. The open circuit voltage and the short-circuit current were calculated using a multimeter. The electrical power was calculated using the relationship power (P) = voltage (V) × current (I).

2.6 Instrumentation

A solar simulator from G2V Optics Inc. (model PICO) which has a maximum 0.7 sun power density was used for the irradiation of the samples. UV-Visible spectra were recorded in the range between 200 and 700 nm with Lab India Analytical (UV 3200). Crystalline structure profiles were analysed by powder X-ray diffraction (XRD) with an InXitu benchtop in spinner mode using Cu Kα radiation. Chemical bonding and functional groups were recognized from the Bruker alpha II Fourier transform infrared spectroscopy analysis. Raman spectra were recorded with a handheld Metrohm Mira P Raman spectrometer. Particle size and Zeta potential values were analysed by Horiba nanopartical SZ-100V2. Real time temperature differences in the means of IR images were captured using a Thermey 256A infrared camera. Scanning Electron Microscopy (SEM) images were obtained on Oxford Instruments Tescan Vega 3 with a resolution of 1.4 nm and at 20 kV electron landing voltage. Samples were gold coated for minimizing charging of samples during SEM imaging by using a sputter device (Q 150R ES, Quorum) with a sputter current of 20 mA for 60 s. SEM imaging of cells was carried out using SEM (EVO 18 Research, Carl Zeiss). High resolution Transmission Electron Microscope images were taken by a JEOL, JEM-2100. Wensar class 1 weighing scales were used to measure the weight loss. All the photo thermal behaviours were analysed using a custom prepared water floater and water evaporator system shown in the schematic image. An inductively coupled plasma optical emission spectrometer (ICP-OES, model ACTIVA S, Horiba Jobin–Yvon) was used for major metal ion concentration analysis.

3. Results and discussion

3.1 Synthesis & characterisation

The GO surface functionalization with TA and loading of Fe^{3+} was carried out through a simple and cost effective sonication assisted wet chemical method stepwise as shown in Fig. 1. The physiochemical properties of the prepared composites were analysed using various techniques and are discussed here. To investigate the absorption properties and interaction of various loading of TA and Fe^{3+} with GO, the UV-Visible spectrum of the synthesised photothermal materials was plotted in Fig. 2(a) with the range of 200–700 nm. For pristine GO the absorption peak was obtained at 235 nm and 300 nm due to the presence of the π–π* transition of sp^2 (C═C) bonds and n–π* (C═O) transition.[26] The addition of Fe^{3+} ions over the GO surface reduces the π–π* transition peak in the form of a red shift to a higher wavelength near 280 nm due to the electron transfer from Fe^{3+} to GO. This red shift increases the efficiency in the form of absorption behaviour of the material towards a longer wavelength. The addition of TA and Fe^{3+} over the GO causes a blue shift towards the visible region of the spectrum.[27] The π–π* transition peak of the TA in the photo thermal materials was blue-shifted from 222 to 216 nm. The re-formation of the conjugated sp^2 carbon domain between GO layers and the oxidation of phenolic moieties in TA and Fe^{3+} were linked to changes in the absorbance peaks of GO and TA. The increase in absorption capabilities in both UV and visible ranges proves the materials efficiency towards strong solar spectrum absorption behaviour.[28] For further understanding the light scattering and absorption properties the refractive index (n) of all the prepared materials were determined and their values are given in Table S2 (ESI†). The refractive index values were 1.6–1.8 suggesting suitability of the materials for photothermal absorption. The structural characterisation of the synthesised GO, GO–Fe^{3+}, TA–Fe^{3+}–GO (PT-2) was carried out using an X-ray diffraction technique and is the results are shown in Fig. 2(b). The diffraction patterns for all the other prepared PT (1–10) are not presented in the graph due to the observance of the same patterns and peak positions for GO with decreased intensity. The changes in peak intensities between pristine GO and GO–Fe^{3+} hybrid nanosheets were clearly visible in this picture. The GO peak was identified at 10.24° along the plane (001) through an interlayer spacing of 0.82 nm, which is consistent with prior findings of graphite to GO.[29] In contrast, Fe^{3+} hybrid GO exhibits a different pattern because the GO peak was lost owing to preferred stacking of Fe^{3+} ions into GO layers, which resulted in lattice imperfection because the dopant Fe^{3+} ion has an ionic radius of 0.069 nm, and it can be found at the GO interstitial site. There is no comparable peak found in the XRD pattern for Fe and the presence of Fe_3O_4.[10] The XRD data revealed that Fe^{3+} ions were doped with GO functional groups *via* substitution. After loading of constant wt% of TA over GO the sharp intensity peak of GO has been slightly broadened and some minor diffraction peaks have appeared at 27° and 42° which resemble

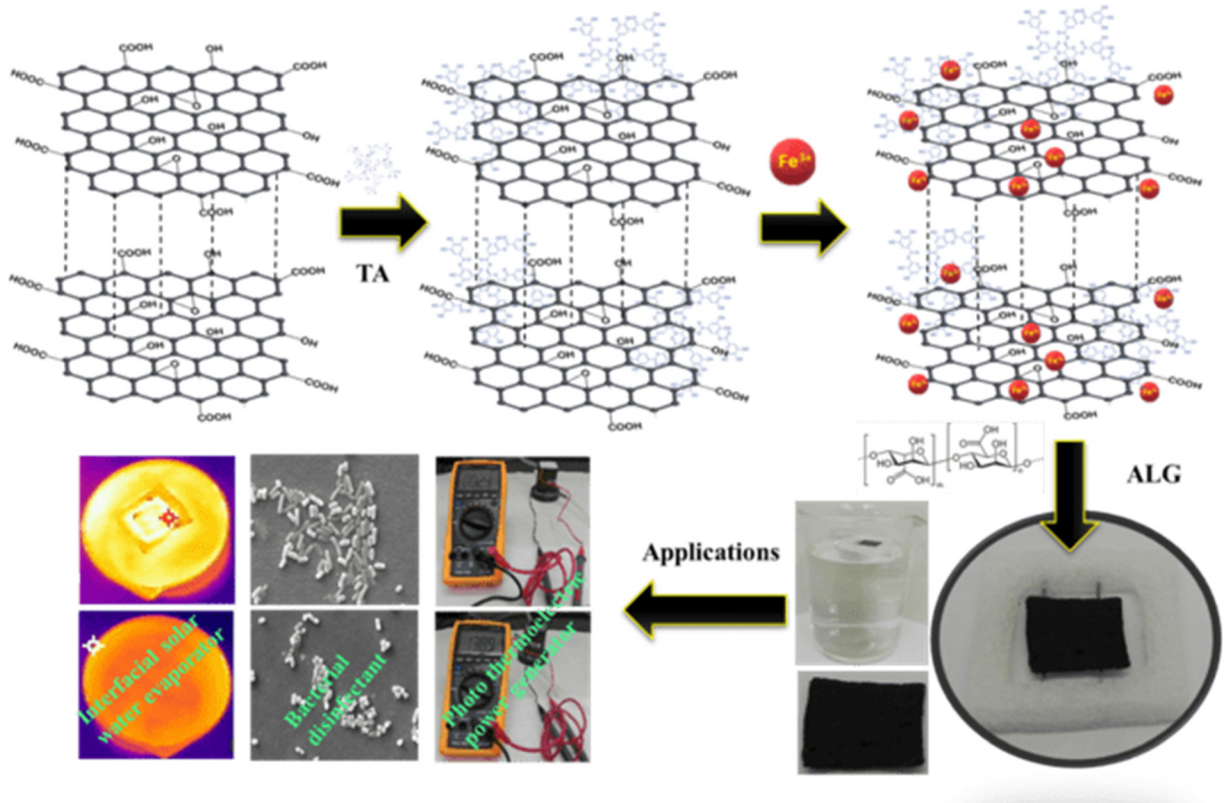

Fig. 1 Schematic for stepwise synthesis and application of the TA–Fe^{3+}–GO–ALG photothermal material.

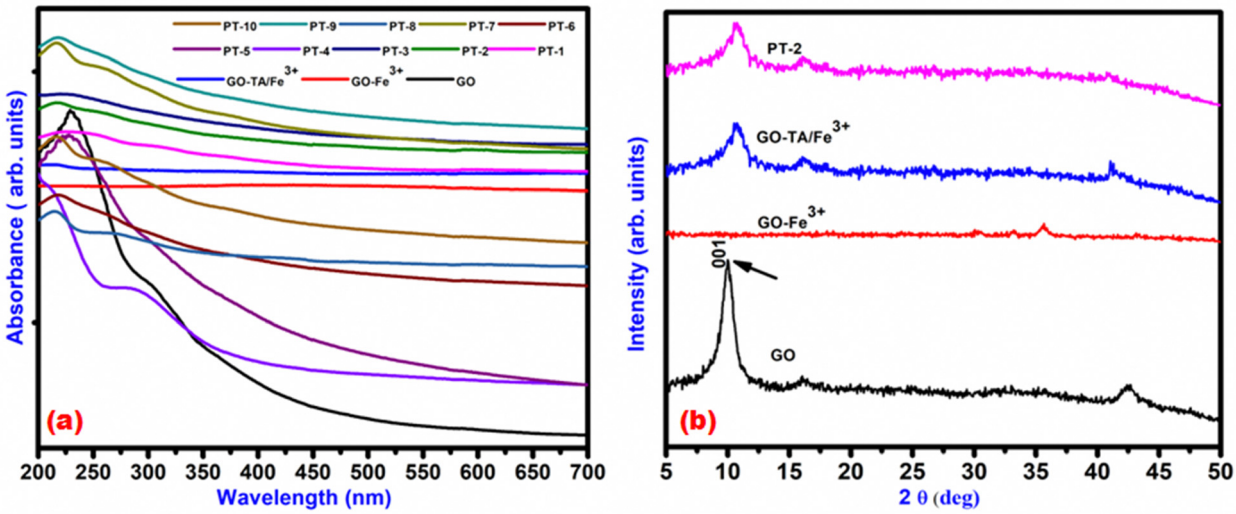

Fig. 2 (a) UV-VIS and (b) XRD pattern of the prepared photothermal materials.

the normal diffraction peak of TA and GO, indicating GO with few layers.[30] Furthermore, unlike the sharp peak of pure GO, the large peak of PT-2 shows disordered stacked GO sheets at the microscopic scale, which is verified by SEM images. Exfoliated layers of GO attempt to restack with a neighbouring layer owing to strong stacking, hydrophobic interaction and van der Waals forces, causing the broad accessible interfaces of graphene sheets to be hampered. TA not only becomes firmly attached onto the graphene surface *via* stacking, endowing graphene with a water suspension ability, but it also converts GO into reduced graphene oxide (RGO) thereby improving chemical stability with π–π interactions. Fig. 3(a) depicts the FT-IR spectra of all the developed photothermal materials. Functional groups such as O–H, C–OH, COOH and C–O were witnessed in all the materials due to the existence of GO and TA.[31] The carboxyl O–H stretching mode is responsible for a large peak between 3500 cm^{-1} and 2500 cm^{-1}. The band at 760 cm^{-1} seen in the spectra of TA–Fe^{3+}–GO indicates the multi-substituted aromatic rings of TA, thereby showing the existence of TA in all the prepared composites. Upon introducing Fe^{3+} to the mixture of GO–TA, the peak at 1346 cm^{-1}, which particularly reflects the C–OH in the plane bending behaviour of the hydroxyl groups in TA, began to fade significantly because of the creation of complexes among hydroxyl groups and Fe^{3+}.[32] The peak at 1619 cm^{-1} is ascribed to C=C stretching from the unoxidized graphitic region. The peak at nearby 1720 cm^{-1} is ascribed to C=O stretching of the carboxyl group and 1224 cm^{-1} resembles the C–OH stretching of the alcohol group and 1080 cm^{-1} is attributed to the C–O stretching vibrations of C–O–C.[33] As seen from Fig. 3(a) (PT-6–PT-10) the intensities of the peaks corresponding to the TA functionalities were enlarged and some new peaks were also recorded. This shows the successful addition of TA over GO. The peaks suggesting the presence of GO were not completely reduced by TA which indicates the presence of both functional groups. The lattice structure and phonon properties of carbon-based materials were seen using Raman spectroscopy. Here, the D and G bands at 1320 cm^{-1} and 1590 cm^{-1} correspond to the tendency of the sp^2 atom's out of plane breathing mode due to defects created while converting from graphite to GO using strong chemical agents and E_{2g} phonons near the core of the Brillion zone, as illustrated in Fig. 3(b). These peaks exhibit the existence of lattice distortion. The ratios of I_D/I_G peak intensities and their corresponding sp^2 crystallite (L) values are given in Table S3 (ESI†) for all the prepared materials which indicates the decrease in average size of sp^2 domains and creation of edge deficiencies owing to the reduction of some C=C bonds in graphene oxide when it comes in contact with TA and Fe^{3+}. The changes in the intensity ratio and increase in the sp^2 crystallite size of the composite materials after the addition of TA and Fe^{3+} provides the evidence of reduction in the oxygen functional group of GO.[34]

The sp^2 crystallite (L) size was calculated by using the following formula:[35]

$$L = 2 \times 10^{-10}(\lambda^4)/(I_D/I_G) \quad (1)$$

Fig. 4(a) shows the SEM images of the prepared GO which seems to be in the stacked layer form and Fig. 4(b) shows the image of the PT-2 photothermal material. Here, the introduction of TA and Fe^{3+} over the surface of the GO makes the layers wrinkle. Most of the particles seem to have sphere-like morphology caused due to the strong contact between the TA and Fe^{3+} with GO functional groups. The increased surface to volume ratio of this nanocomposite with various sharp edged surface makes it more active. Energy dispersive X-ray spectrometry (EDS) analysis along with elemental mapping was carried out for the TA–Fe^{3+}–GO–ALG (PT-2) material and it was observed that all the structural elements C, O and Fe were uniformly present over the GO surface. Uniform loading of Fe^{3+} is ensured from the Fe distribution mapping and the O and C presence is because of both GO and TA. The result is presented in the ESI† (Fig. S1). The HR-TEM images are depicted in Fig. 5.

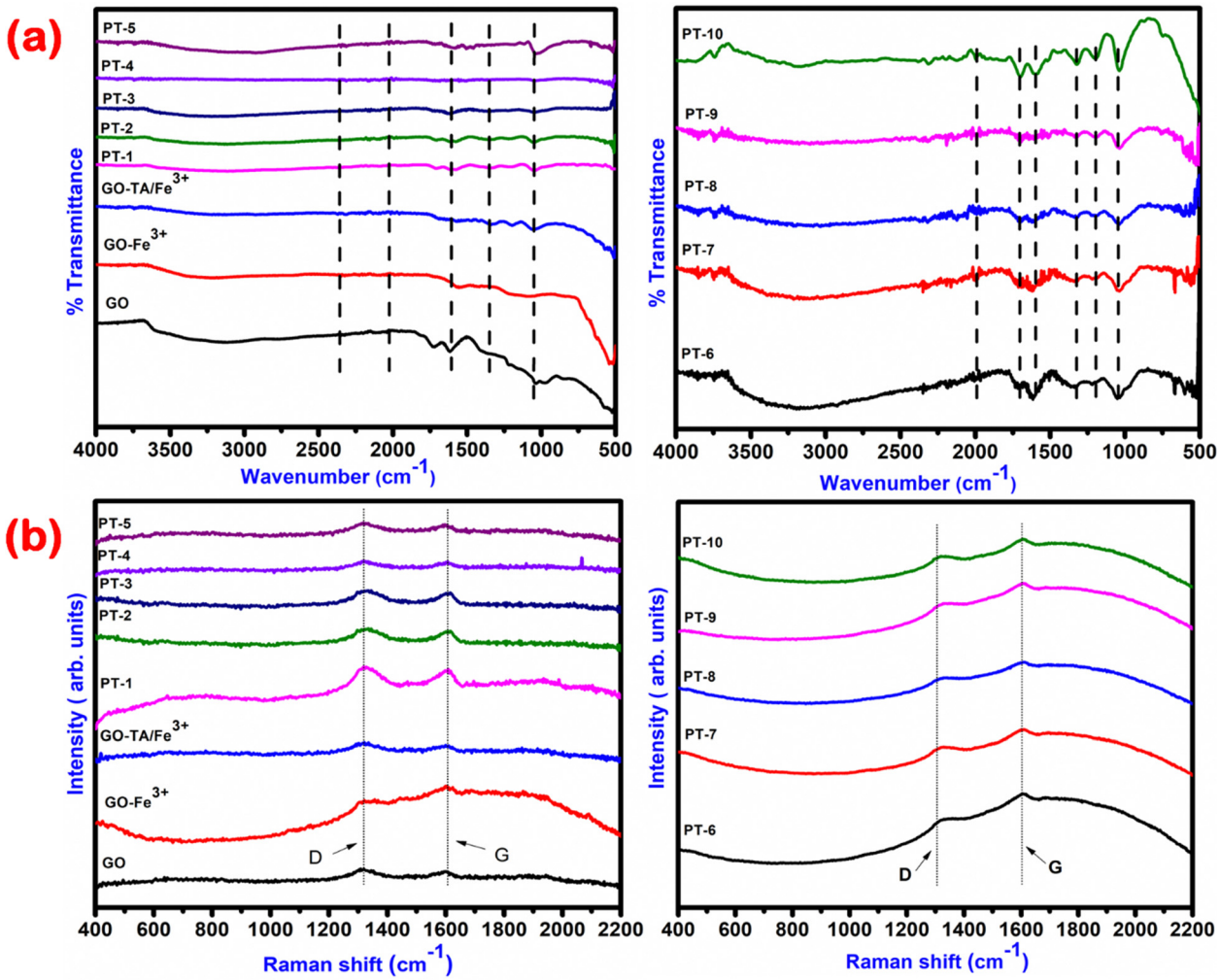

Fig. 3 (a) FTIR spectrum and (b) Raman spectrum of the prepared photothermal materials.

Fig. 5(a) shows the TEM image of GO and Fig. 5(b) shows the TEM of PT-2. The presence of a thin layer structure of GO can be observed and the coating of TA and Fe^{3+} is also seen as small dark spots on the TEM [Fig. 5(b)]. The TEM images suggest that TA and Fe^{3+} were embedded over the layer of GO. Zeta potential measurement at different pH was carried out for GO, TA–GO, Fe^{3+}–GO and PT-2 materials as shown in Fig. S2 (ESI†). GO, Fe^{3+}–GO, and TA–GO and the PT-2 material show negative surface charges above pH 2. The partial neutralisation of the negative surface potential of GO is observed in Fe^{3+}–GO due to incorporation of Fe^{3+} ions into the layers which have a positive surface charge. Secondly, the effect of incorporation of TA into GO is seen by the increase in negative surface potential. The surface charge of PT-2 is affected by the combined effect of positive Fe^{3+} and negative TA overall making it slightly more negative than GO throughout the pH range. The DLS size distribution yielded a mean diameter of 3.4 μm for GO and 6.6 μm for the PT-2 material. Size distribution is plotted in the ESI† (Fig. S3). Although spherical particle approximation does not remain accurate for the GO type structure, a positive shift of the size distribution after Fe^{3+} and TA loading suggest an overall increase in size after their incorporation into GO. Alternative characterization techniques were utilised for verifying the structural changes before and after exposure of the photothermal material. The surface and crystal structures before and after exposure to 1 sun illumination was verified using SEM images and XRD patterns. SEM observations suggest that there was no visible structural change and XRD analysis suggests that the crystal structure was not disturbed due to exposure. The results are provided in the ESI† (Fig. S4a and b).

3.2 Photo thermal performance assessment

The most efficient setup for generating water vapour is an interfacial heating-based evaporation system, which confines heat to the interface between air–liquid and it doesn't transfer heat to the bulk water. This process of steam generation saves time and energy and the mode of operation makes it a user-friendly device. Following that, we investigated the photothermal abilities through various parameters of the fabricated floating materials. A stable and well-organized photothermal transformation capability is critical for determining whether this material can be utilized for solar water evaporation. The

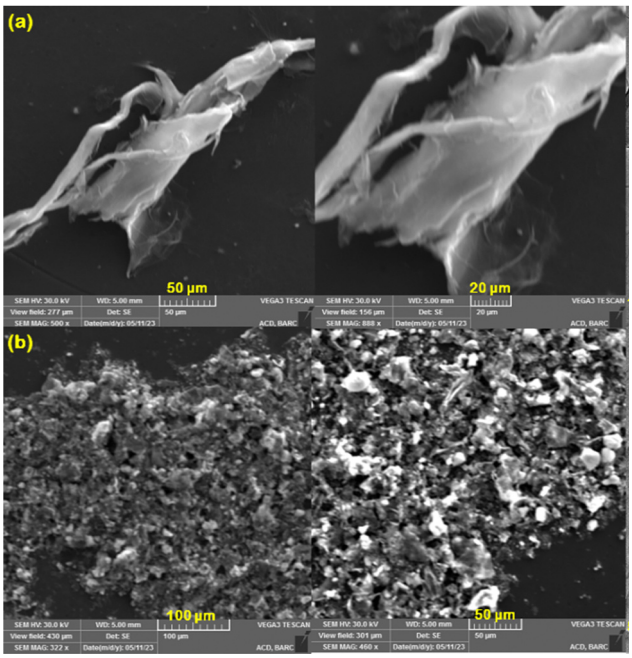

Fig. 4 SEM images of (a) GO and (b) PT-2.

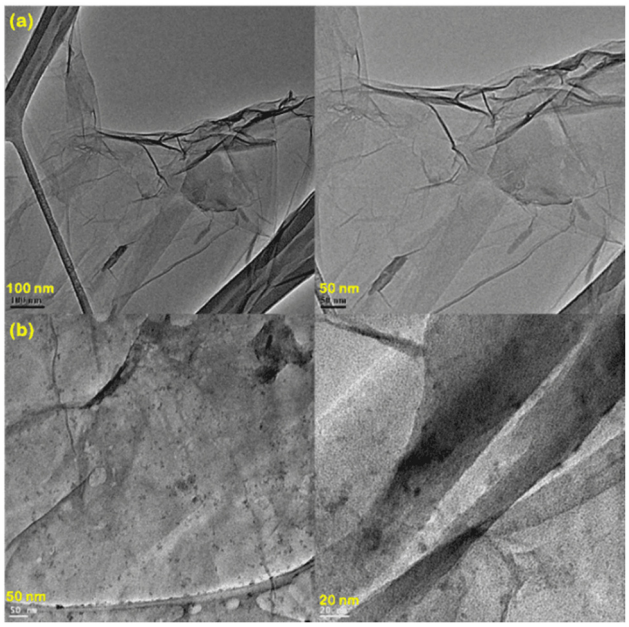

Fig. 5 HR-TEM images of (a) GO and (b) PT-2.

developed photothermal material TA–Fe^{3+}–GO–ALG has an intertwined nature which creates numerous open microscopic channels throughout the layer and it serves as capillary pathways for water at the air–water interface. This phenomenon maximizes water transport and enables quick replenishment of evaporated surface water. Initially, these materials were illuminated under 0.5 sun for different time intervals from 0 s to 300 s and their heat generation capability is shown in Fig. 6. Fig. 6(a) shows the water temperature and Fig. 6(b) shows the increase in water temperature. After absorption of light the heat conversion process results in increased temperature which can be visually seen through the IR camera. Interestingly, the heat passage from the PT material to the surrounding water can be seen in Fig. 7. The pure GO which behaves as an insulator material in this present work prevents the whole composite material acting as a dedicated photothermic material and its functionalization's absorb broadly over the whole light spectrum in order to capture as much solar energy as feasible. As seen from the SEM images, the wrinkled nature with multiple shapes and dimensions acts as active sites as thermal generators within the whole system. The increase in temperature of pristine GO and Fe^{3+}–GO from normal room temperature to 30 °C and 34 °C respectively can be visualised. The plasmon resonance properties of Fe^{3+} are activated owing to the incoming light and delocalized electrons of Fe^{3+} collectively excite and result in hot electrons in this process. The heated electrons vibrate in time along with the input electromagnetic field and it produces heat and transfer throughout the graphene crystal lattices.[36] The inclusion of TA over GO and coating with Fe^{3+} materials temperature rises to 37 °C, which is suggestively greater than that of pure GO and Fe^{3+}–GO. The heat generated is limited to the direct air–water interface, and the rest of the evaporation system remains at the environment's temperature (<25 °C). Despite the external temperature being much less than the steady-state temperature in the dry state shown in the schematic of the synthesis procedure. To assess the effect of TA and Fe^{3+} loadings, two different sets of material composites were synthesized namely (PT-1 to PT-5) and (PT-6 to PT-10) and their wt% are given in Table S1 in the ESI.† Efficient photo thermal conversion and water evaporation take place on the floaters PT-2 and other PT 6–10 materials. Here, the PT-2 material consists of 0.5 : 1 : 2 loading values which show that 2 wt% of Fe precursor provide a good distribution of Fe^{3+} over the TA and at the same time the increased loading of TA from 0.1 to 0.5 wt% in the materials PT-5 to PT-10 shows a similar temperature which doesn't show any significant role of TA with constant Fe^{3+} at 2 wt%. The interfacial air water zone of the PT-2 material causes the water to evaporate quickly as a result of the high heat conversion zone, resulting in a rapid light to heat conversion efficiency. Although surface vapour takes away a considerable quantity of heat in the course of the evaporation process, water from beneath the floater quickly replenishes it *via* capillary action. This reduces heat loss *via* radiation and convection to the surrounding environment, eventually improving the solar energy utilization efficiency. The optical picture of normal water with and without evaporator was obtained and presented inside the schematic image (Fig. 1). The water evaporation performance of the photothermal materials was then evaluated by measuring the changes in the mass of water as a function of light illumination time. Eqn (2) was used to determine the light to heat conversion efficiency.[37]

$$\eta = \frac{\frac{dm}{dt \times S} \times He}{Q_s} \times 100\% \quad (2)$$

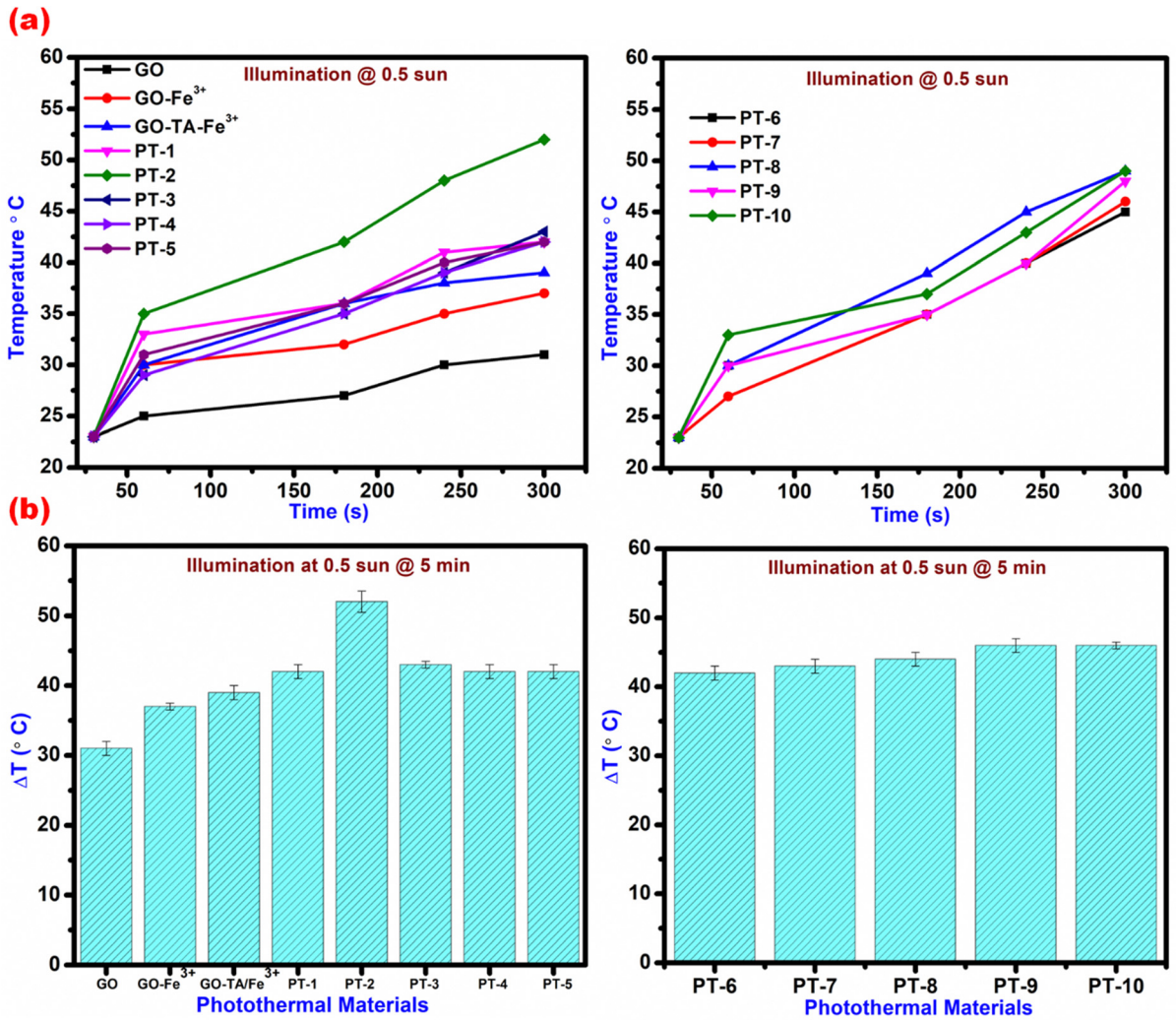

Fig. 6 Increase in temperature of water illuminating TA–Fe^{3+}–GO–ALG at various time intervals (a) absolute temperature; (b) change in temperature.

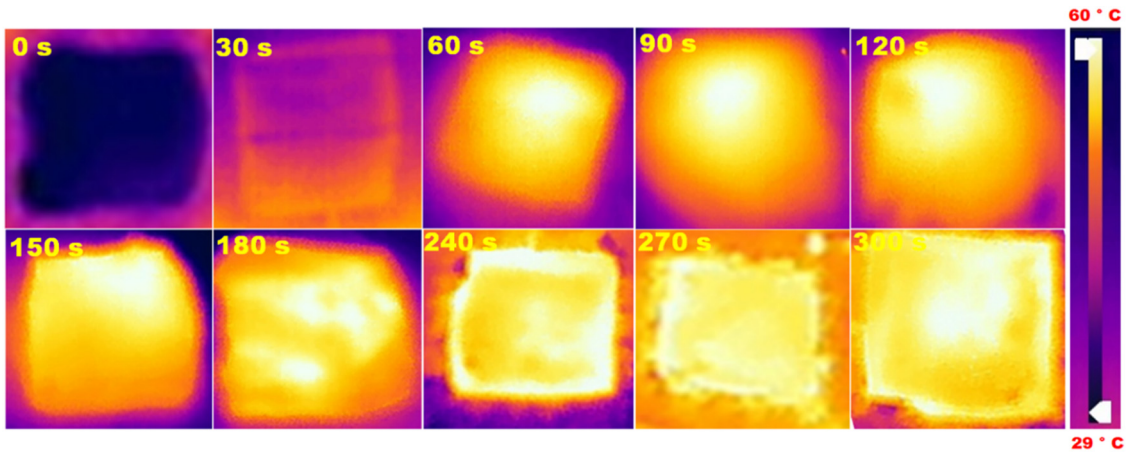

Fig. 7 Water temperature profile using TA–Fe^{3+}–GO–ALG (PT-2). Changes in temperature at different time intervals.

where, m is the mass of vaporized water, t is the time, S is the surface area, He is the heat of evaporation of water ($\sim$2260 kJ kg^{-1}), and Q_s is the power density of the light source (500 W m^{-2}). The mass loss of water and the water evaporation rate are shown in Fig. 8(a) and (c) for all the prepared materials. Here, the PT-2 demonstrates a high water evaporation rate of

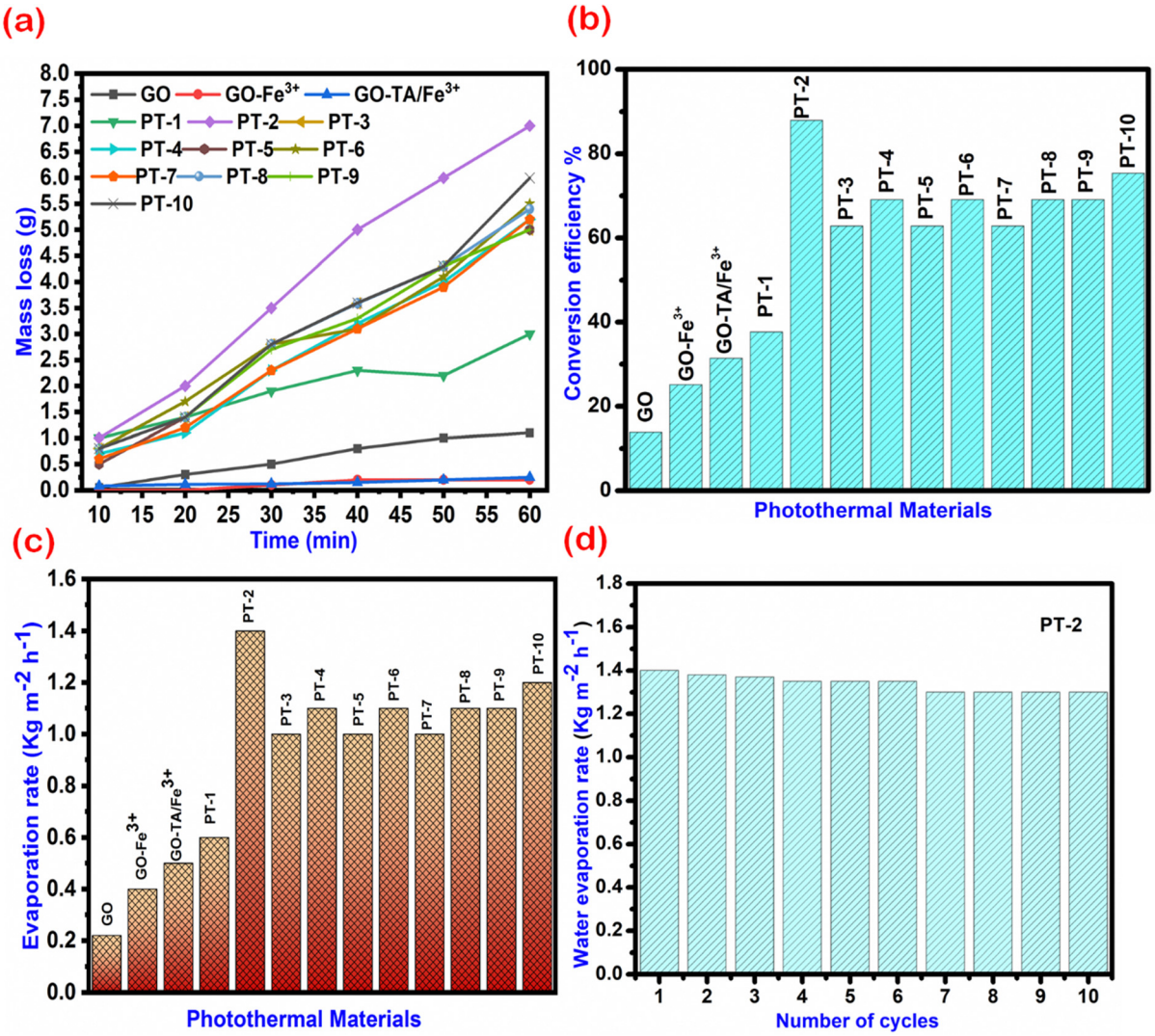

Fig. 8 Photo thermal behaviour of the prepared TA–Fe^{3+}–GO–ALG photothermal material. (a) Mass loss of water regrading 0.5 sun illumination, (b) calculated conversion efficiency, (c) evaporation rate, and (d) evaporation rate of the PT-2 material for different cycles.

up to 1.4 kg m^{-2} h^{-1} under 0.5 sun illumination. An experiment conducted under 1 kW m^{-2} irradiation intensity yielded 1.8 kg m^{-2} h^{-1} evaporation rate. This is significantly higher than the evaporation rates of GO (0.2 kg m^{-2} h^{-1}) and GO–Fe^{3+} (0.4 kg m^{-2} h^{-1}) conducted under similar illumination conditions. The water evaporation efficiency of the materials is shown in Fig. 8(b) and it maintains a good evaporation rate for ten cycles as tested with the PT-2 material [Fig. 8(d)]. The efficiency of PT-2 is calculated to be 87%, which is one of the best values reported.

As also observed from the temperature profiles in Fig. 9 [(a) thermal profile; (b) increase in temperature], the temperature of the TA–Fe^{3+}–GO–ALG (PT-2) along with the surrounding water increases with illumination intensity. The maximum temperature achieved with 2 sun irradiation was >70 °C. The light-to-heat conversion efficiency and water evaporation rate under different solar illumination conditions were measured.[38–40] Fig. 9c shows the evaporation rates from 0.05 sun to 2 sun illumination conditions using TA–Fe^{3+}–GO–ALG (PT-2). The evaporation efficiencies were plotted in Fig. 9d for different illuminations. It was clear from Fig. 9c and d that the detection limit for the TA–Fe^{3+}–GO–ALG (PT-2) for effective photothermal conversions is close to 0.2 sun. The outdoor solar irradiation intensity varies from 0.5 sun to 2 sun depending on the location, timing of the day and the weather conditions. The 0.5 sun intensity at which most of the experiments were carried out is a conservative one available even during overcast conditions. It was however demonstrated from the 0.2 sun detection limit that the developed TA–Fe^{3+}–GO–ALG (PT-2) photothermal material can also work under heavily overcast conditions.

3.3 Water purification using the TA–Fe^{3+}–GO–ALG photothermal material

Methyl red, methyl orange and rhodamine-b were the dyes taken as model organic pollutants in 100 mL of ground water

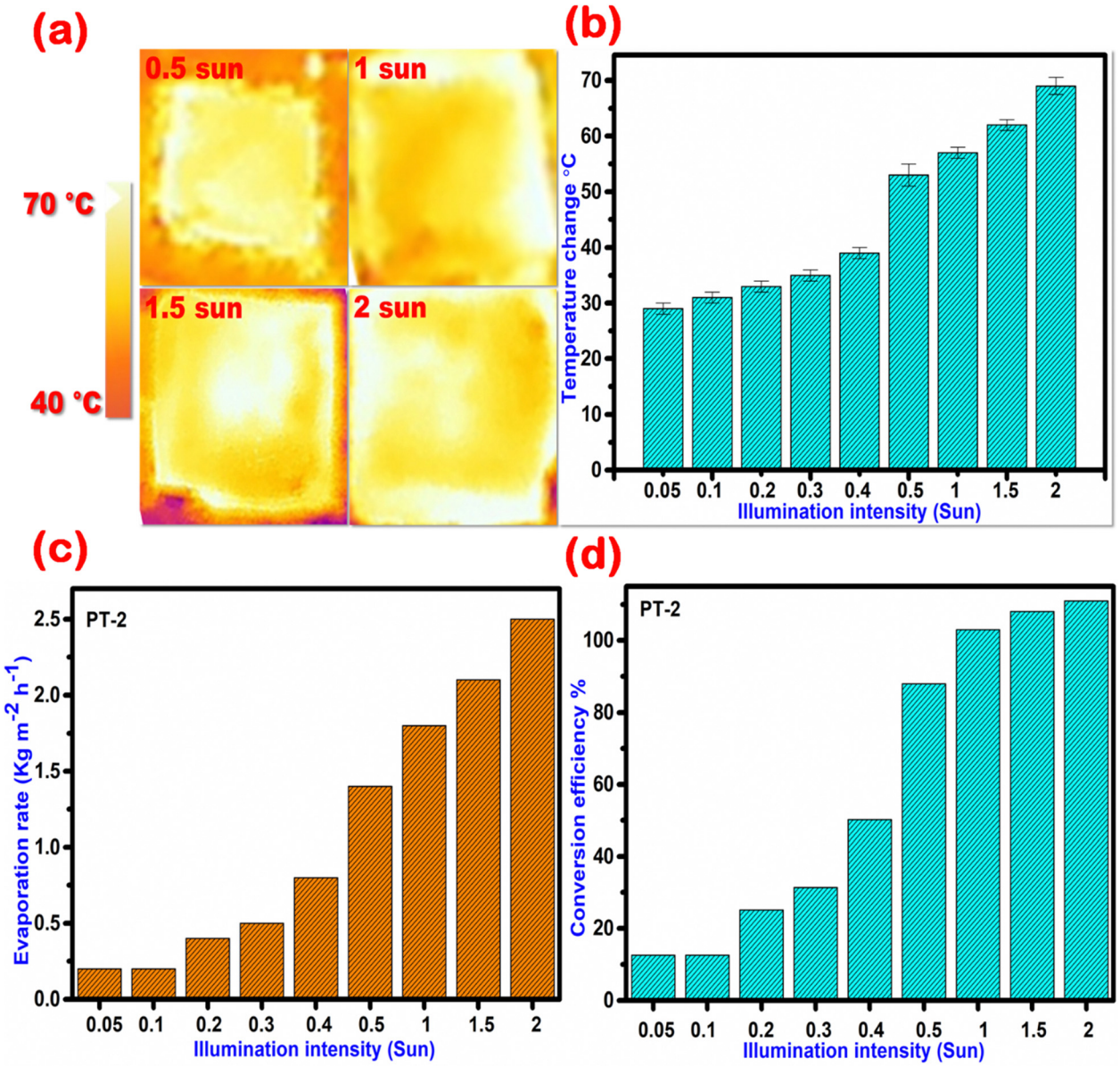

Fig. 9 Photo thermal behaviour of the prepared TA–Fe^{3+}–GO–ALG (PT-2) material under various illumination conditions. (a) Thermal profile, (b) temperature increase, (c) evaporation rate, and (d) conversion efficiency.

and methyl orange dye was added to the sea water and lake water. The pH of the solutions was adjusted as per the discussion given above in Section 2.3. Preceding the illumination by light, the dyes were continuously stirred under dark conditions for 15 min to attain an adsorption–desorption equilibrium state. The photo thermal material TA–Fe^{3+}–GO–ALG (PT-2) was allowed to float over the dye mixed water and the illumination (0.5 sun) was given for the water evaporation experiment. Finally the collected fresh water was analysed by using a UV-Vis spectrophotometer and their absorption profiles are shown in Fig. 10. Fig. 10(a) presents the UV-VIS absorption pattern of groundwater spiked with three different dyes before and after condensation. Fig. 10(b) shows the same water spiked with methyl orange but under acidic and basic conditions. Fig. 10(c) presents methyl orange spiked lake water and sea water. The collected evaporated water is shown which seems to be transparent in colour and the pH of the collected fresh water was around 7. The above results reveal that PT-2 can efficiently evaporate the freshwater from waste water and sea water, lake water and the freshwater collected satisfies WHO criteria for human consumption.

3.4 Antimicrobial properties of the TA–Fe^{3+}–GO–ALG photothermal material

Spot assays as well as viability counts indicated the superior antimicrobial properties of TA–Fe^{3+}–GO–ALG (PT-2) material. Following 4 h of treatment no growth was observed as shown in Fig. 11(a)–(c) which correlated with the negligible CFU counts.

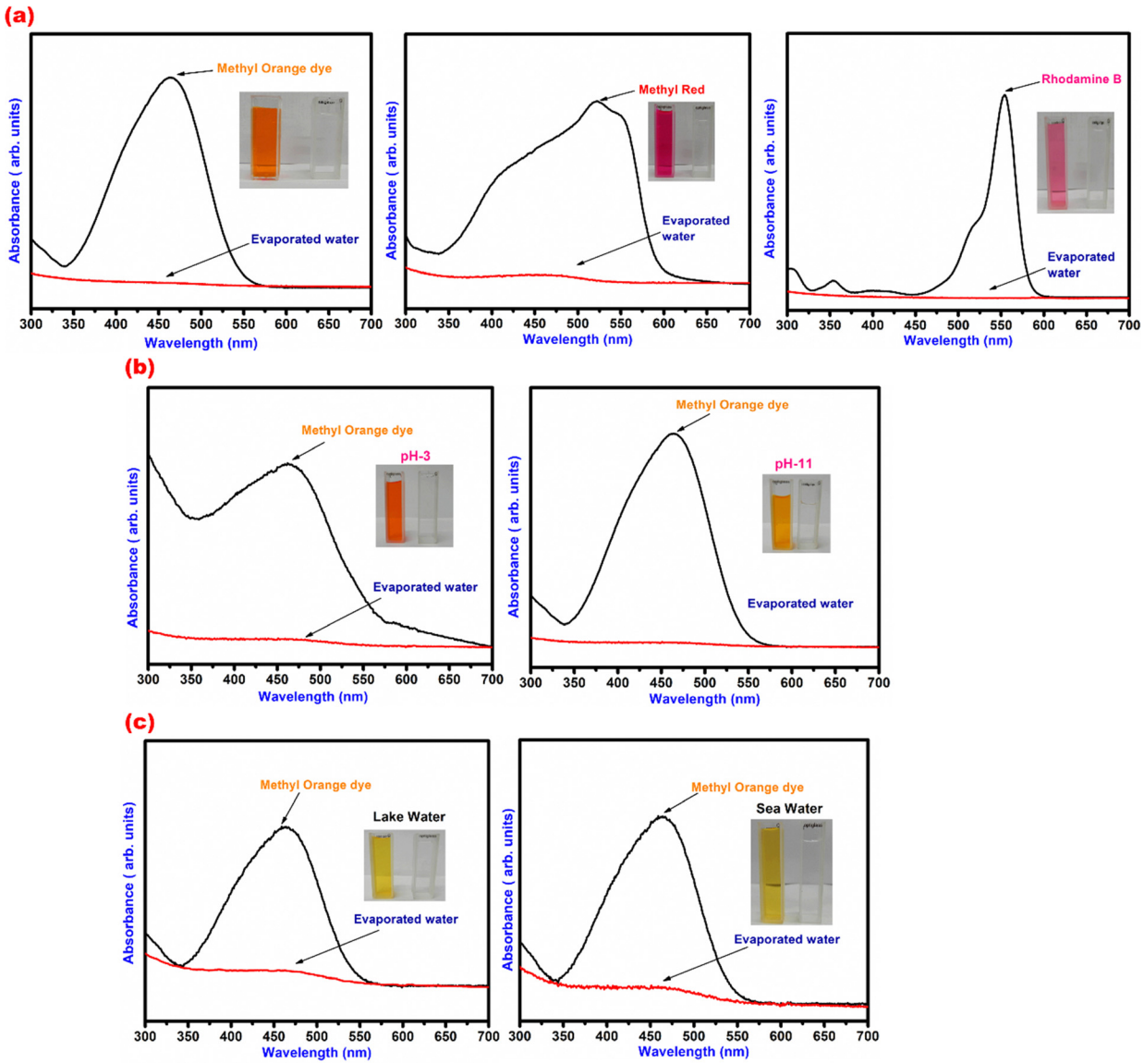

Fig. 10 UV-VIS absorption pattern of model pollutants. (a) Underground water added with dyes, (b) underground water added with methyl orange dye at different pH conditions, and (c) methyl orange dye added to lake water and sea water.

Table 1 represents the CFU counts at 0 h and 4 h of treatment which concurs with the viability data [Fig. 11(a)–(c)]. SEM was employed for visualization of surface morphological changes following 4 h of treatment with TA–Fe^{3+}–GO–ALG (PT-2). It was observed that the cells exhibited damaged cell surfaces and the cell aggregation after 4 h of treatment as compared to the control cells. These damaged cells were not viable (Table 1) and did not result in colony formation [Fig. 11(b)].

3.5 Electric power generation using the photo-thermoelectric effect

When the light shines on the TA–Fe^{3+}–GO–ALG (PT-2) material, a wide spectrum of light undergoes multiple exchanges such as scatterings and reflections within the material and lastly gets trapped inside the nanostructure.[41,42] Consequently, the incident energy of the photon will be translated into heat, causing temperature escalation on the surface of the TA–Fe^{3+}–GO–ALG material. This method of solar-to-thermal conversion is known as the photothermal process. When integrated with the thermoelectric module, it can cause electric power generation *via* the photo-thermoelectric effect and is an effective methodology to meet the impending global energy crisis.[43,44] Fig. 10 displays the working principle of photo-thermoelectric power generation using a Bi_2Te_3 based thermoelectric module coupled with the TA–Fe^{3+}–GO–ALG material under solar radiation. Fig. 10 in the ESI,† displays the photograph of the integrated assembly. In typical solar energy harvesting through the photo-thermoelectric effect, the light absorbing TA–Fe^{3+}–GO–ALG material converts solar light into thermal energy, leading to a rise in temperature on the top surface of the thermoelectric module, while the bottom surface of the module remains at a lower temperature. Thus, the temperature gradient (ΔT)

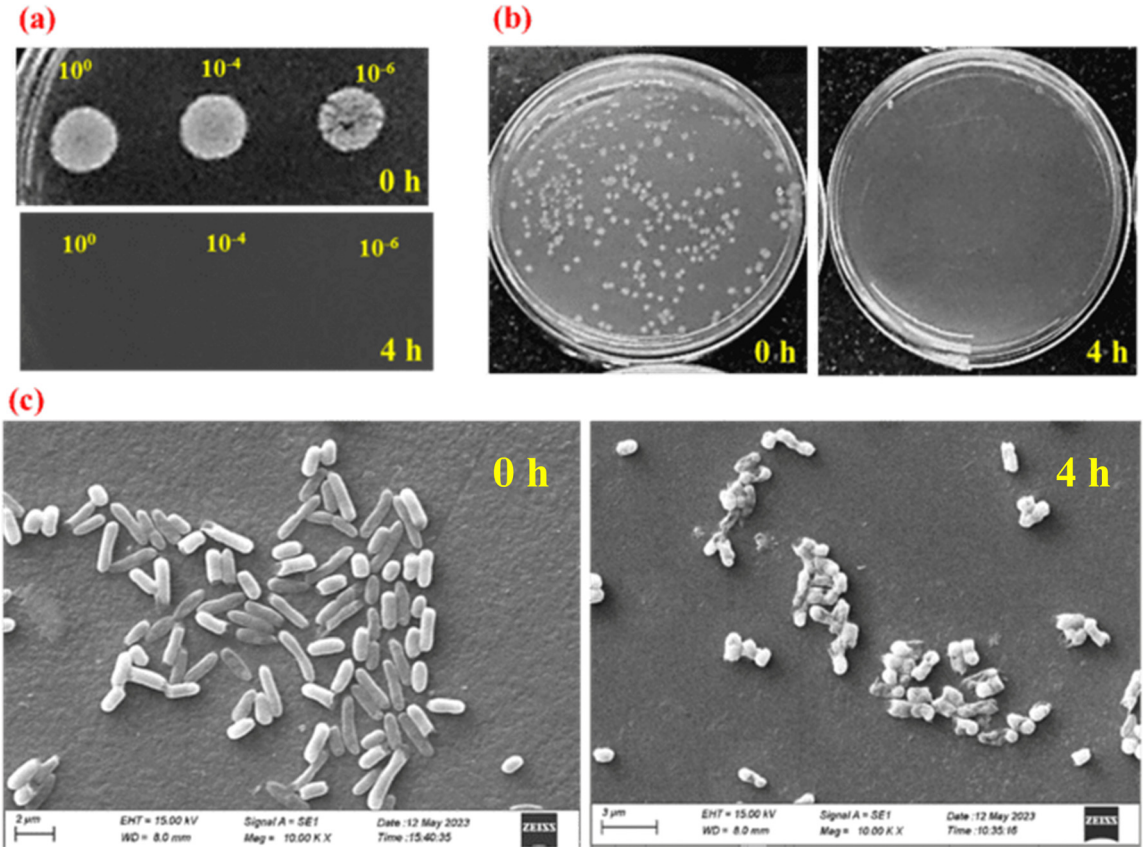

Fig. 11 Antimicrobial assays: representative (a) spot assays and (b) CFU counts of *E. coli* cells following 0 h and 4 h of treatment with PT-2 and (c) the corresponding SEM images at 10 000× magnification.

Table 1 Viability of *E. coli* (CFU mL^{-1}) before and after treatment with TA–Fe^{3+}–GO–ALG (PT-2)

CFU mL^{-1}	0 h	4 h
PT-2 – 0 h	$(2.26 \pm 0.41) \times 10^8$	—

between the top and bottom end of the thermoelectric module drives the separation of the charge carriers within the p- and n-type thermoelements. Consequently, the Seebeck voltage increases and thereby is easily measured using a multimeter.

By measuring the open-circuit voltage and the short-circuit current with and without the light absorbing material, the performance of the integrated device based on the photo-thermoelectric effect can be realized. Fig. 12(a) and (b) represent the change in the open-circuit voltage and the short-circuit current with the exposure time. It is to be noted that the open-circuit voltage enhances briskly in the initial minutes and thereafter shows a steady value of 138 ± 4 mV. This can be attributed to the fact that the light absorber attains thermal equilibrium with the ambience. Nevertheless, the open-circuit voltage drops rapidly when the light is switched off. Similarly, the short-circuit current also shows a similar trend. The maximum steady current value is 221 mA. Thus, the maximum power calculated is 30.72 mW and the corresponding power density is 1.92 mW cm^{-2}. The stability test was carried out and the result indicates an appreciably high power output. However, it is to be noted that to improve the solar-to-electricity conversion a large temperature gradient needs to be maintained across both the surfaces of the thermoelectric module.

3.6 Sustainability study

To demonstrate the practical performance, this prepared TA–Fe^{3+}–GO–ALG (PT-2) was employed for a seawater evaporation process using the sample sea water. The outdoor evaporation experiment was done on a sunny day in the month of May 2023 and its evaporation rate from 10:00 h to 17:00 h is given in Fig. 13a. The whole experiment shows the difference in amount of collected fresh water with the peak water evaporation rate at noon time due to the availability of more solar irradiation. The availability of solar light in the Mumbai region will be up to 7 pm which causes the performance of the evaporation rate to be stable and slightly saturated after 3–4 pm. The distillation performance mentioned here is far superior to that of typical solar distilling machines. A schematic representation of the evaporation and condensation set up used in this study is shown in Fig. 13b. The concentrations of five primary ions from real seawater and evaporated water were determined by using inductively coupled plasma optical emission spectrometry and ion chromatography (ICP-OES and IC). After the

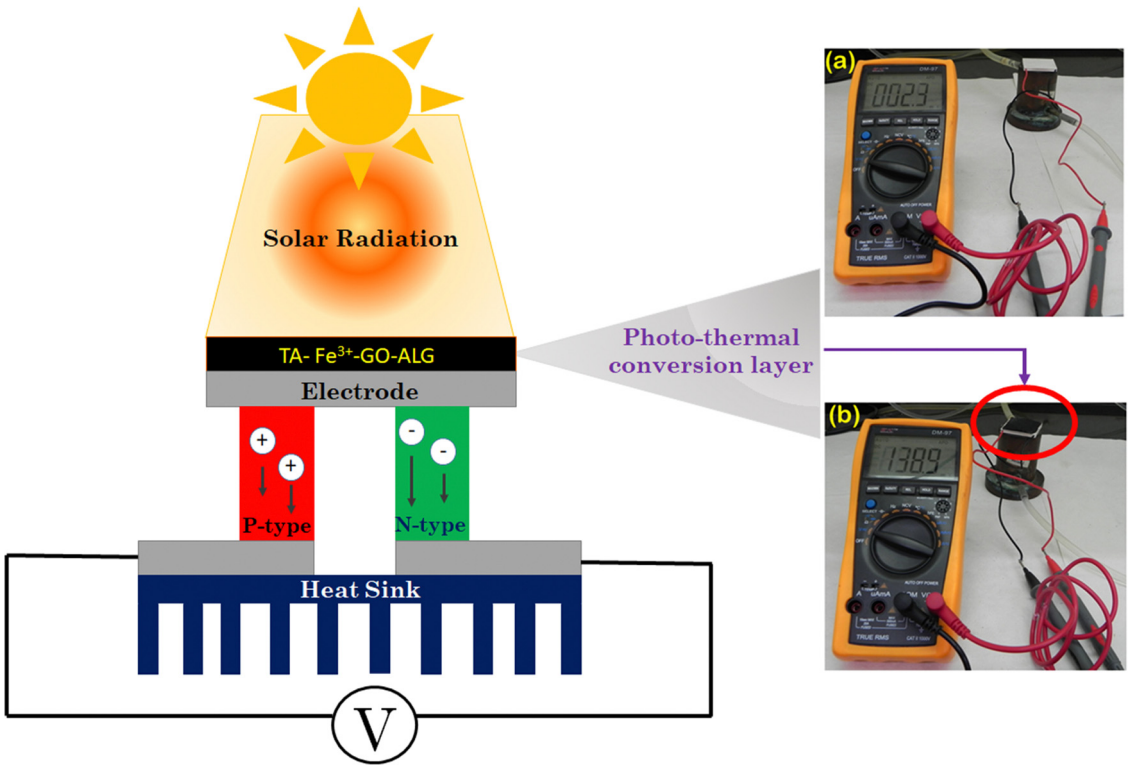

Fig. 12 Open-circuit voltage and the short-circuit current (a) without TA–Fe^{3+}–GO–ALG (PT-2) and (b) with the TA–Fe^{3+}–GO–ALG (PT-2) material.

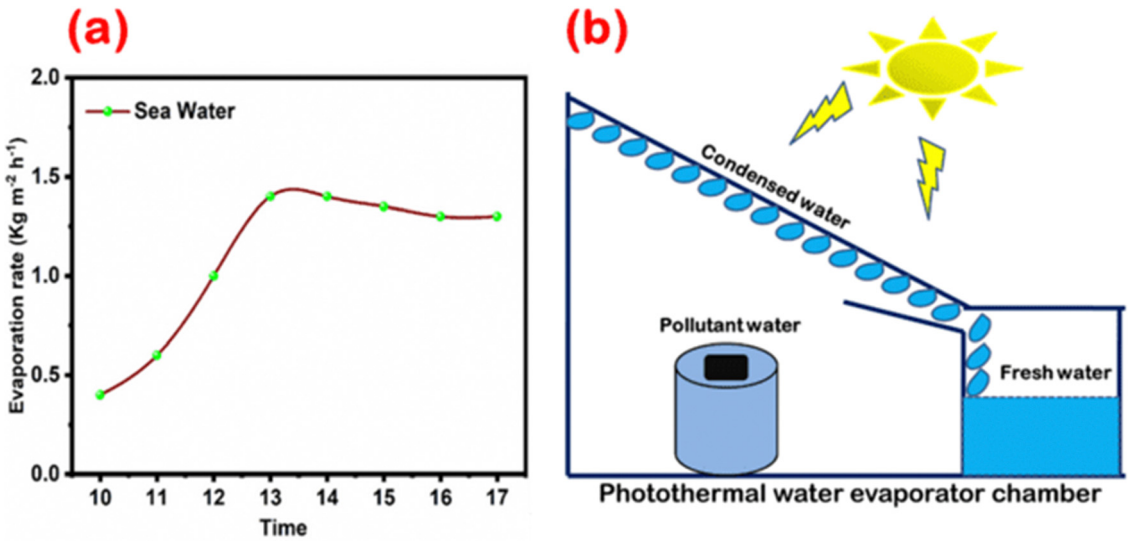

Fig. 13 (a) Water evaporation rate of TA–Fe^{3+}–GO–ALG (PT-2) at day times (10–17 h) and (b) a schematic image of the water evaporator chamber.

photothermal evaporation process, the collected fresh water consists of negligible concentrations of these ions as shown in Table 2 which are well below the minimum threshold standard approved by the U.S. Environmental Protection Agency and the World Health Organization. The initial concentration of the major ions is also tabulated in Table 2. This demonstrates a superior performance compared to thermal distillation (1–50 ppm) and membrane-based (10–500 ppm) techniques. A comparison of the developed material [TA–Fe^{3+}–GO–ALG (PT-2)] has been drawn in Table 3 with the already reported materials in terms of photothermal materials efficiency, evaporation rate and photo-thermoelectric power generation capability (power density). These results show great potential for practical solar desalination and power generation using the TA–Fe^{3+}–GO–ALG (PT-2) material. Most notably, this PT material doesn't require any noble metals or delicate nanotechnology

Table 2 Concentration of ions before and after water evaporation using the TA–Fe^{3+}–GO–ALG (PT-2) water floater

S. no.	Primary ions in real sea water	Concentration before evaporation ($\mu g\ mL^{-1}$)	Concentration in collected freshwater ($\mu g\ mL^{-1}$)
1	Na^+	2081	2.37
2	Ca^{2+}	88.99	1.07
3	Fe	0.07	0.002
4	K^+	238.4	0.14
5	Cl^-	3480	2.3

treatment, making it more cost-effective than the majority of previously reported materials.[45,46] Antimicrobial properties and probable thermoelectric material integrated power generation make TA–Fe^{3+}–GO–ALG (PT-2) a versatile photothermal material.

3.7 Probable photothermal conversion mechanism

Upon irradiation by the solar light locally on the surface of the photothermal material TA–Fe^{3+}–GO–ALG (PT-2) prominently three different forms of processes will begin instantly to take place precisely, absorption, scattering and reflection. From the refractive index calculation, we have seen that the value is very close to 2 which means that it can be a good absorptive material. In this current context, only absorption will support the light to heat generation process. GO is known to be a good broad solar light absorber which can undergo a series of photophysical effects and diffuse it to the neighbouring components TA and Fe^{3+}. When the energy of the incoming light satisfies the bandgap of the nanostructure it will transit from the ground state to the excited state. The accurate bandgap calculation however involves rigorous density functional theory calculation (DFT) which may not be feasible for a complex system like TA–Fe^{3+}–GO–ALG (PT-2). Usage of two different organic structures GO and TA enhances the heat conversion process owing to the transition of electrons within molecules. At the same time, TA functional groups will have electrons occupying the lowest excited singlet state *via* vibrational relaxation and an internal conversion mechanism.[63] The role of alginate is to provide the framework with necessary pathways for efficient water transmission through capillary action and quick steam escape. There will be competing processes like reoccurrence to the ground state *via* fluorescence emission and other processes through non-radiative transition as heat generation. The photothermal effect of TA–Fe^{3+}–GO–ALG (PT-2) may be attributed to the occurrence of the multiple non-radiative transitions arising from the favourable band structure.

4. Conclusions

In this study, we analysed and established the multifunctional roles of the tannic acid–Fe^{3+}–graphene oxide impregnated alginate photothermal network (TA–Fe^{3+}–GO–ALG). Various loadings of TA and Fe^{3+} over the GO layer followed by loading into the alginate matrix were optimised for construction of a photothermal water floater material. The TA–Fe^{3+}–GO–ALG photothermal material exhibited a benchmark light to heat conversion efficiency of 87% and 1.8 kg m^2 h^{-1} rate of water evaporation under 1 sun solar illumination. Remarkable solar energy harvesting properties coupled with excellent stability, recyclability, and no photo leaching were manifested in a 70 °C increase of water temperature, producing clean water from simulated waste water and sea water indicating great feasibility for its implementation as a solar water purifier. The TA–Fe^{3+}–GO–ALG material also showed exceptional antibacterial efficacy towards *E. coli*, eradicating nearly 100% of bacteria when exposed to 0.5 solar irradiation. The excellent photo-thermal conversion efficiency integrated with a commercial thermoelectric module exhibited a good photo-thermoelectric effect yielding a maximum steady current value of 221 mA with a corresponding power density of 1.92 mW cm^{-2}. Overall, TA–Fe^{3+}–GO–ALG is a benchmark photothermal material with

Table 3 Comparison of conversion efficiency, evaporation rate and power density with those of previously reported photothermal materials

Material	Light illumination intensity (KW m^{-2})	Conversion efficiency (%)	Evaporation rate (kg m^{-2} h^{-1})	Power density (W m^{-2})	Ref.
rGO–mixed cellulose esters	1	75	0.838	—	47
rGO–MWCNT	1	80.4	1.22	—	48
GO–PVA	1	92	1.63	—	49
rGO–SA–TiO_2	1	96	1.63	—	50
GO–melamine	1	86	1.35	0.9	51
rGO–hydroxyapattite nanowires	1	89.2	1.48	—	52
MXene/cellulose	1	94	1.44	—	53
MWCNTs–ZrO_2–Ni@CQDs	1	89.5	1.95	—	54
PC-x hydrogel	1	97.2	3.52	0.65	55
Monolith 3D xerogel	1	87	3.39	0.63	56
CNT/CNF films	3	84.5	1.23	310[a]	57
MnO_2@PPy NC		—	1.69	12.3	58
Poly(ethylene terephthalate)	1	—	2.49	0.8	59
Fe_3O_4–PPy	2	—	1.98	45.4	60
CBP–CuO	1	105.3	1.72	57.459[a]	61
NF@RGO–CNT	1	96.4	1.37	0.251	62
TA–Fe^{3+}–GO–ALG (PT-2)	1	87	1.8	1.92	This work

[a] Output voltage in mV.

interfacial water evaporation, antimicrobial properties, and photo-thermoelectric effect for sustainable energy and environmental applications.

Author contributions

M. Amarnath: methodology, synthesis, investigation, data acquisition, visualisation, and writing – original draft preparation; Hirakendu Basu: visualisation, conceptualization, writing – reviewing and editing, and supervision; Ranita Basu: solar irradiation, investigation of the photo-thermoelectric properties, and validation; Pallavi Chandwadkar: antimicrobial study; Celin Acharya: antimicrobial property investigation, and data interpretation; Shweta Singh: methodology, investigation, and characterisation; Suresh Kumar Kailasa: visualisation, interpretation, and conceptualization; Chandra Nath Patra: administration, resources, fund acquisition, project management, and supervision.

Conflicts of interest

The authors have no conflicts of interest to declare.

Acknowledgements

The authors sincerely express their gratitude for the continuous guidance and support provided by Prof. A. K. Tyagi, Director, Chemistry Group, BARC.

References

1 H. Chen, S. L. Wu, H. L. Wang, Q. Y. Wu and H. C. Yang, Photothermal devices for sustainable uses beyond desalination, *Adv. Energy Sustainability Res.*, 2021, **2**, 2000056.
2 H. Ma and M. Xue, Recent advances in the photothermal applications of two-dimensional nanomaterials: photothermal therapy and beyond, *J. Mater. Chem. A*, 2021, **9**, 17569–17591.
3 X. Zhao, X. Meng, H. Zou, Y. Zhang, Y. Ma, Y. Du, Y. Shao, J. Qi and J. Qiu, Nano-enabled solar driven-interfacial evaporation: Advanced design and opportunities, *Nano Res.*, 2023, **16**, 6015–6038.
4 H. Fayaz, S. Rasachak, M. S. Ahmad, L. Kumar, B. Zhang, M. A. Mujtaba, M. E. Soudagar, R. Kumar and M. R. Omidvar, Improved surface temperature of absorber plate using metallic titanium particles for solar still application, *Sustain. Energy Technol. Assess.*, 2022, **52**, 102092.
5 N. J. Baygi, S. M. Beidokhti and M. M. Ghafoorian, Cu-Mn mixed-component oxide nanoparticles synthesized *via* the one-step solution combustion method with enhanced water evaporation efficiency, *J. Aust. Ceram. Soc.*, 2023, **3**, 795–809.
6 H. Zhang, L. Li, L. Geng, X. Tan, Y. Hu, P. Mu and J. Li, Reduced graphene oxide/carbon nitride composite sponge for interfacial solar water evaporation and wastewater treatment, *Chemosphere*, 2023, **311**, 137163.
7 M. S. Irshad, Y. Hao, N. Arshad, M. Alomar, L. Lin, X. Li, S. Wageh, O. A. Al-Hartomy, A. G. Al-Sehemi, V. D. Dao and H. Wang, Highly charged solar evaporator toward sustainable energy transition for in-situ freshwater & power generation, *Chem. Eng. J.*, 2023, **15**, 141431.
8 J. Y. Wang, X. X. Guo, J. Chen, S. C. Hou, H. J. Li, A. Haleem, S. Q. Chen and W. D. He, A versatile platform of poly (acrylic acid) cryogel for highly efficient photothermal water evaporation, *Mater. Adv.*, 2021, **2**, 3088–3098.
9 X. Cui, Q. Ruan, X. Zhuo, X. Xia, J. Hu, R. Fu, Y. Li, J. Wang and H. Xu, Photothermal Nanomaterials: A Powerful Light-to-Heat Converter, *Chem. Rev.*, 2023, **123**, 6891–6952.
10 W. Yang, W. Hu, J. Zhang, W. Wang, R. Cai, M. Pan, C. Huang, X. Chen, B. Yan and H. Zeng, Tannic acid/Fe^{3+} functionalized magnetic graphene oxide nanocomposite with high loading of silver nanoparticles as ultra-efficient catalyst and disinfectant for wastewater treatment, *Chem. Eng. J.*, 2021, **405**, 126629.
11 W. Yang, H. Hu, Q. Pan, X. Deng, Y. Zhang and Z. Shao, Iron-polydopamine coated multifunctional nanoparticle SiO_2@PDA/Fe^{3+}-FA mediated low temperature photothermal for chemodynamic therapy of cisplatin-insensitive osteosarcoma, *Mater. Des.*, 2023, **227**, 111785.
12 S. Singh, H. Basu, M. V. Pimple and R. K. Singhal, Synthesis of PEI functionalized silica microsphere loaded polymeric network for simultaneous removal of Cr (III) & Cr (VI) from aquatic medium, *Mater. Today Commun.*, 2023, **35**, 105706.
13 S. Singh, H. Basu, M. K. Bassan and R. K. Singhal, Thiol functionalised silica microsphere loaded polymeric hydrogel: Development of a novel hybrid sorbent for removal of lead and cadmium, *Chemosphere*, 2022, **286**, 131659.
14 S. Saha, H. Basu, M. Venkatesh, S. Singh and R. K. Singhal, Synthesis and characterization of noble hydrogel beads of amino functionalized reduced graphene oxide for selective extraction of gold from electronic waste, *Mater. Today Commun.*, 2022, **33**, 104371.
15 H. Basu, S. Singh, S. Kumar Kailasa and R. Kumar Singhal, Application of Core–Shell Nanohybrid Structures in Water Treatment, *Nanohybrid Materials for Water Purification*, 2022, pp. 279–316.
16 B. Tan, M. Sun, B. Liu, X. Jiang, Q. Feng, E. Xie, P. Xi and Z. Zhang, Boosting photocarrier collection in semiconductors by synergizing photothermoelectric and photoelectric, *Nano Energy*, 2023, **107**, 108138.
17 M. N. Sarker, M. L. Raihan, M. E. Huq, M. M. Kamruzzaman, T. Chumky and T. Hattori, Ways of Water Management in Islam: Potential Insights for Future Water Governance, *Indigenous and Local Water Knowledge, Values and Practices*, 2023, pp. 47–65.
18 X. Xu, H. Lv, M. Zhang, M. Wang, Y. Zhou, Y. Liu and D. G. Yu, Recent progress in electrospun nanofibers and their applications in heavy metal wastewater treatment, *Front. Chem. Sci. Eng.*, 2023, 1–27.
19 M. Lindmark, K. Cherukumilli, Y. S. Crider, P. Marcenac, M. Lozier, L. Voth-Gaeddert, D. S. Lantagne, J. R. Mihelcic, Q. M. Zhang, C. Just and A. J. Pickering, Passive in-line

chlorination for drinking water disinfection: a critical review, *Environ. Sci. Technol.*, 2022, **56**, 9164–9181.

20 N. Parveen, S. Chowdhury and S. Goel, Environmental impacts of the widespread use of chlorine-based disinfectants during the COVID-19 pandemic, *Environ. Sci. Pollut. Res.*, 2022, 1–19.

21 F. S. Awad, H. D. Kiriarachchi, K. M. AbouZeid, U. Ozgur and M. S. El-Shall, Plasmonic graphene polyurethane nanocomposites for efficient solar water desalination, *ACS Appl. Energy Mater.*, 2018, **1**, 976–985.

22 L. Noureen, Z. Xie, Y. Gao, M. Li, M. Hussain, K. Wang, L. Zhang and J. Zhu, Multifunctional Ag_3PO_4-rGO-coated textiles for clean water production by solar-driven evaporation, photocatalysis, and disinfection, *ACS Appl. Mater. Interfaces*, 2020, **12**, 6343–6350.

23 X. Wang, G. Ou, N. Wang and H. Wu, Graphene-based recyclable photo-absorbers for high-efficiency seawater desalination, *ACS Appl. Mater. Interfaces*, 2016, **8**, 9194–9199.

24 P. Cheng, D. Wang and P. Schaaf, A review on photothermal conversion of solar energy with nanomaterials and nanostructures: From fundamentals to applications, *Adv. Sustainable Syst.*, 2022, **6**, 2200115.

25 X. Guan, P. Kumar, Z. Li, T. K. Tran, S. Chahal, Z. Lei, C. Y. Huang, C. H. Lin, J. K. Huang, L. Hu and Y. C. Chang, Borophene Embedded Cellulose Paper for Enhanced Photothermal Water Evaporation and Prompt Bacterial Killing, *Adv. Sci.*, 2023, **10**, 2205809.

26 Y. J. Kim, H. Choi, C. S. Kim, G. Lee, S. Kim, J. Park, S. E. Park and B. J. Cho, High-performance monolithic photovoltaic–thermoelectric hybrid power generator using an exothermic reactive interlayer, *ACS Appl. Energy Mater.*, 2019, **2**, 2381.

27 F. Dimroth, M. Grave, P. Beutel, U. Fiedeler, C. Karcher, T. N. Tibbits, E. Oliva, G. Siefer, M. Schachtner, A. Wekkeli and A. W. Bett, Wafer bonded four-junction GaInP/GaAs//GaInAsP/GaInAs concentrator solar cells with 44.7% efficiency, *Prog. Photovolt. Res. Appl.*, 2014, **22**, 277.

28 X. Han, Z. Wang, M. Shen, J. Liu, Y. Lei, Z. Li, T. Jia and Y. Wang, A highly efficient organic solar energy-absorbing material based on phthalocyanine derivative for integrated water evaporation and thermoelectric power generation application, *J. Mater. Chem. A*, 2021, **9**, 24452.

29 P. Cheng and D. Wang, Easily Repairable and High-Performance Carbon Nanostructure Absorber for Solar Photothermoelectric Conversion and Photothermal Water Evaporation, *ACS Appl. Mater. Interfaces*, 2023, **15**, 8761.

30 X. Liu, P. Zhao, C. Y. He, W. M. Wang, B. H. Liu, Z. W. Lu, Y. F. Wang, H. X. Guo, G. Liu and X. H. Gao, Enabling Highly Enhanced Solar Thermoelectric Generator Efficiency by a CuCrMnCoAlN-Based Spectrally Selective Absorber, *ACS Appl. Mater. Interfaces*, 2022, **14**, 50180.

31 L. Zhu, T. Ding, M. Gao, C. K. Peh and G. W. Ho, Shape conformal and thermal insulative organic solar absorber sponge for photothermal water evaporation and thermoelectric power generation, *Adv. Energy Mater.*, 2019, **9**, 1900250.

32 D. C. Marcano, D. V. Kosynkin, J. M. Berlin, A. Sinitskii, Z. Sun, A. Slesarev, L. B. Alemany, W. Lu and J. M. Tour, Improved synthesis of graphene oxide, *ACS Nano*, 2010, **4**, 4806.

33 M. K. Rabchinskii, V. V. Shnitov, A. T. Dideikin, A. E. Aleksenskii, S. P. Vul', M. V. Baidakova, I. I. Pronin, D. A. Kirilenko, P. N. Brunkov, J. Weise and S. L. Molodtsov, Nanoscale perforation of graphene oxide during photoreduction process in the argon atmosphere, *J. Phys. Chem. C*, 2016, **120**, 28261.

34 H. Ozawa and M. A. Haga, Soft nano-wrapping on graphene oxide by using metal–organic network films composed of tannic acid and Fe ions, *Phys. Chem. Chem. Phys.*, 2015, **17**, 8609.

35 N. Bensalah, K. Chair and A. Bedoui, Efficient degradation of tannic acid in water by UV/H_2O_2 process, *Sustain. Environ. Res.*, 2018, **28**, 1.

36 N. M. Huang, H. N. Lim, C. H. Chia, M. A. Yarmo and M. R. Muhamad, Simple room-temperature preparation of high-yield large-area graphene oxide, *Int. J. Nanomed.*, 2011, **19**, 3443.

37 Y. B. Kwon, S. H. Go, C. Choi, T. H. Seo, B. Yang, M. W. Lee and Y. K. Kim, Simultaneous reduction and functionalization of graphene oxide sheets with tannic acid for a strong composite material with multi-modally interactive interfaces, *Diamond Relat. Mater.*, 2021, **119**, 108565.

38 L. Sang, W. Hao, Y. Zhao, L. Yao and P. Cui, Highly aligned graphene oxide/waterborne polyurethane fabricated by in-situ polymerization at low temperature, *e-Polymers*, 2018, **18**, 75–84.

39 M. Namvar-Mahboub, E. Khodeir and A. Karimian, Preparation of magnetically recoverable Fe_3O_4–graphene oxide catalyst by green method and its application for reduction of nitropyrimidine in aqueous medium, *Res. Chem. Intermed.*, 2018, **44**, 6877.

40 A. F. Santos, L. J. Macedo, M. H. Chaves, M. Espinoza-Castañeda, A. Merkoçi, F. D. Lima and W. Cantanhêde, Hybrid self-assembled materials constituted by ferromagnetic nanoparticles and tannic acid: A theoretical and experimental investigation, *J. Braz. Chem. Soc.*, 2016, **27**, 727.

41 H. Fan, L. Wang, X. Feng, Y. Bu, D. Wu and Z. Jin, Supramolecular hydrogel formation based on tannic acid, *Macromolecules*, 2017, **50**, 666.

42 S. Nam, M. W. Easson, B. D. Condon, M. B. Hillyer, L. Sun, Z. Xia and R. Nagarajan, A reinforced thermal barrier coat of a Na–tannic acid complex from the view of thermal kinetics, *RSC Adv.*, 2019, **9**, 10914.

43 J. Luo, N. Zhang, J. Lai, R. Liu and X. Liu, Tannic acid functionalized graphene hydrogel for entrapping gold nanoparticles with high catalytic performance toward dye reduction, *J. Hazard. Mater.*, 2015, **300**, 615.

44 N. Kumar and V. C. Srivastava, Simple synthesis of large graphene oxide sheets *via* electrochemical method coupled with oxidation process, *ACS Omega*, 2018, **3**, 10233.

45 M. S. Irshad, N. Arshad and X. Wang, Nanoenabled photothermal materials for clean water production, *Glob. Challenges*, 2021, **5**, 2000055.

46 R. Meng, J. Lyu, L. Zou, Q. Zhong, Z. Liu, B. Zhu, M. Chen, L. Zhang and Z. Chen, CNT-based gel-coated cotton fabrics for constructing symmetrical evaporator with up/down inversion property for efficient continuous solar desalination, *Desalination*, 2023, **554**, 116494.

47 G. Wang, Y. Fu, X. Ma, W. Pi, D. Liu and X. Wang, Reusable reduced graphene oxide based double-layer system modified by polyethylenimine for solar steam generation, *Carbon*, 2017, **114**, 117.

48 Y. Wang, C. Wang, X. Song, S. K. Megarajan and H. Jiang, A facile nanocomposite strategy to fabricate a rGO–MWCNT photothermal layer for efficient water evaporation, *J. Mater. Chem. A*, 2018, **6**, 963.

49 L. Chen, J. Wei, Q. Tian, Z. Han, L. Li, S. Meng and Q. M. Hasi, Dual-functional graphene oxide-based photothermal materials with aligned channels and oleophobicity for efficient solar steam generation, *Langmuir*, 2021, **37**, 10191.

50 W. Dong, Y. Wang, Y. Zhang, X. Song, H. Peng and H. Jiang, Bilayer rGO-Based Photothermal Evaporator for Efficient Solar-Driven Water Purification, *Chem. – Eur. J.*, 2021, **27**, 17428.

51 A. Ghaffar, Q. Imran, M. Hassan, M. Usman and M. U. Khan, Simultaneous solar water desalination and energy generation by high efficient graphene oxide-melanin photothermal membrane, *J. Environ. Chem. Eng.*, 2022, **10**, 108424.

52 Z. C. Xiong, Y. J. Zhu, D. D. Qin and R. L. Yang, Flexible salt-rejecting photothermal paper based on reduced graphene oxide and hydroxyapatite nanowires for high-efficiency solar energy-driven vapor generation and stable desalination, *ACS Appl. Mater. Interfaces*, 2020, **12**, 32556.

53 X. J. Zha, X. Zhao, J. H. Pu, L. S. Tang, K. Ke, R. Y. Bao, L. Bai, Z. Y. Liu, M. B. Yang and W. Yang, Flexible anti-biofouling MXene/cellulose fibrous membrane for sustainable solar-driven water purification, *ACS Appl. Mater. Interfaces*, 2019, **11**, 36589.

54 R. T. Ginting, H. Abdullah, E. Taer, O. Purba and D. Perangin-angin, Novel strategy of highly efficient solar-driven water evaporation using MWCNTs-ZrO_2-Ni@ CQDs composites as photothermal materials, *Colloids Surf., A*, 2022, **642**, 128653.

55 J. Ren, L. Chen, J. Gong, J. Qu and R. Niu, Hofmeister effect mediated hydrogel evaporator for simultaneous solar evaporation and thermoelectric power generation, *Chem. Eng. J.*, 2023, **458**, 141511.

56 L. Chen, J. Ren, J. Gong, J. Qu and R. Niu, Cost-effective, scalable fabrication of self-floating xerogel foam for simultaneous photothermal water evaporation and thermoelectric power generation, *Chem. Eng. J.*, 2023, **454**, 140383.

57 Y. Li, J. Wang, C. Fu, L. Huang, L. Chen, Y. Ni and Q. Zheng, Designing flexible CNT/CNF films with highly light-absorbing for solar energy harvesting: Seawater desalination, photothermal power generation and light-driven actuators, *Energy Convers. Manage.*, 2023, **289**, 117160.

58 M. S. Irshad, X. Wang, N. Arshad, M. Q. Javed, T. Shamim, Z. Guo and T. Mei, Bifunctional in situ polymerized nanocomposites for convective solar desalination and enhanced photo-thermoelectric power generation, *Environ. Sci.: Nano*, 2022, **9**(5), 1685–1698.

59 B. Chen, J. Ren, Y. Song, P. He, H. Bai, Z. Fan and J. Gong, Upcycling waste poly (ethylene terephthalate) into a porous carbon cuboid through a MOF-Derived carbonization strategy for interfacial solar-driven water–thermoelectricity cogeneration, *ACS Sustainable Chem. Eng.*, 2022, **10**(49), 16427–16439.

60 M. S. Irshad, Y. Hao, N. Arshad, M. Alomar, L. Lin, X. Li and H. Zhang, Highly charged solar evaporator toward sustainable energy transition for in-situ freshwater & power generation, *Chem. Eng. J.*, 2023, **458**, 141431.

61 J. Li, M. Liu, Y. Cui, W. Luo, Y. Jing, G. Xing and A. Li, Catkins based flexible photothermal materials for solar driven interface evaporation collaborative power generation, *Surf. Interfaces*, 2023, 103170.

62 Z. Chen, X. Li, R. Liu, K. Ma, H. Sang, Y. Huang and C. Tang, Nickel Foam@ Reduced Graphene Oxide–Carbon Nanotube Composite as an Efficient Solar Evaporator for Water Purification and Electricity Generation, *Ind. Eng. Chem. Res.*, 2022, **61**(44), 16565–16576.

63 J. Li, W. Zhang, W. Ji, J. Wang, N. Wang, W. Wu and L. Li, Near infrared photothermal conversion materials: Mechanism, preparation, and photothermal cancer therapy applications, *J. Mater. Chem. B*, 2021, **9**(38), 7909–7926.